LASER INTERFEROMETER GRAVITATIONAL WAVE OBSERVATORY
- LIGO -
CALIFORNIA INSTITUTE OF TECHNOLOGY
MASSACHUSETTS INSTITUTE OF TECHNOLOGY

Technical Note	**LIGO-T2400259–v2**	2024/09/08

2024 LIGO SURF Final Report: 40m ALS / SFG

Dhatri Raghunathan

California Institute of Technology
LIGO Project, MS 18-34
Pasadena, CA 91125
Phone (626) 395-2129
Fax (626) 304-9834
E-mail: info@ligo.caltech.edu

Massachusetts Institute of Technology
LIGO Project, Room NW22-295
Cambridge, MA 02139
Phone (617) 253-4824
Fax (617) 253-7014
E-mail: info@ligo.mit.edu

LIGO Hanford Observatory
Route 10, Mile Marker 2
Richland, WA 99352
Phone (509) 372-8106
Fax (509) 372-8137
E-mail: info@ligo.caltech.edu

LIGO Livingston Observatory
19100 LIGO Lane
Livingston, LA 70754
Phone (225) 686-3100
Fax (225) 686-7189
E-mail: info@ligo.caltech.edu

http://www.ligo.caltech.edu/

Contents

1 Abstract

The LIGO detectors, which are designed to measure the incredibly small disturbances caused by passing gravitational waves, must maintain a stable locked configuration. LIGO and its 40m prototype locks and stabilizes the primary laser to the arm cavity by using an auxiliary (AUX) laser as a reference. Noise budgeting catalogs all relevant noise sources to explain the observed noise, enabling targeted improvements to enhance the interferometer's stability and sensitivity. The first phase of the project aims to identify contributors to the noise spectrum through noise budgeting.

The LIGO Voyager upgrade aims to enhance high-frequency sensitivity by using high-power operation and highly squeezed vacuum states, with a strict squeezing loss budget requiring quantum efficiency (QE) of at least 99% at the 2 µm operating wavelength. Sum-frequency generation (SFG) offers an alternative to improve photodetection QE by upconverting 2 µm fields to 700 nm, allowing the use of traditional photodetectors like InGaAs or Si with QE of $\geq$ 99%. The second phase of the project is to demonstrate a single pass of SFG using a PPLN crystal and a pump of 1064 µm.

2 Introduction

The LIGO (Laser Interferometer Gravitational-Wave Observatory) detectors are essentially large scale Michelson interferometers which are designed to sense variations in space-time strain induced by passing Gravitational Waves (GWs). The LVK (LIGO-Virgo-KAGRA) detector network currently consists of two Advanced LIGO detectors in the U.S.; the Advanced Virgo detector in Italy; and the Japanese detector, KAGRA. A third Advanced LIGO detector is to be located in India.

The 40m prototype of LIGO at Caltech is a 1:100 scale model of the LIGO facility. It serves as a testing ground for upgrades aimed at enhancing the Advanced LIGO (aLIGO) detectors. The primary objective of this project is to study the implementation of upgrades that significantly improve the sensitivity of the GW detectors. Currently, the detector faces challenges related to quantum efficiency (QE) in photodetection and laser feedback stabilization.

3 Arm Length Stabilization

The X and Y arms are 4-km long, Fabry-Perot cavities formed by the highly reflective end test masses and partially transmissive input test masses. Pre-stabilized laser (PSL) light enters the detector from the left, and is further stabilized using an input mode cleaner optical cavity. Cleaned light then enters the Power Recycling Cavity (formed by a partially transmissive input coupler and two high reflectors), is split by a 50/50 beamsplitter, and sent into the long arm cavities where the light interacts most with the potentially changing gravitational field. The light returning from the arm cavities interferes at the beamsplitter, and is then extracted from the beamsplitter's antisymmetric port by the Signal Recycling Cavity (SRC), similarly formed by two high reflectors and a partially transmissive output coupler. Finally, light exiting the SRC is cleaned with an additional resonant cavity, referred

to as the "output mode cleaner". Faraday Isolators (FI) are used for optical isolation of the main interferometer from the rest of the instrument. The transmitted light of the output mode cleaner is split onto two photodiodes, whose output current is turned to voltage, conditioned, digitized, de-conditioned digitally, and then linearly combined to form derr.

Laser feedback stabilization plays a crucial role in maintaining stable optical cavity lengths, and decreasing the time required to get back to the observing state in case the locking breaks. The Arm Length Stabilization (ALS) system employs auxiliary frequency doubled Nd-YAG lasers to sense the lengths of the fabry-perot cavities in the arms independent of the rest of the interferometer. This ALS readout is used to suppress the residual arm motions to less than 1nm rms, and also detune the arm cavities off resonance with the primary science laser, so that the central degrees of freedom can be locked. Enhancing this system for laser locking holds the potential to increase the number of detections significantly ($\sim$1 per week) due to increase in the time the detector is in observing mode. Previous work on ALS at the 40m lab has focused on feasibility and initial implementations of a digital control system.

Ultimately, the goal is to reduce the ALS noise in order to achieve a much more stable locked IFO state faster. This system has many underlying loops in place which contribute to the RMS or noise spectrum. Identification of the noise contributors is the most crucial step in this process - which is why noise budgeting is so important. It is basically making a catalog of all relevant noise terms in order to explain the observed noise.

The golden triad of Noise Budgeting:

- Noise measurements: collecting data from individual sources under same experimental conditions
- Transfer Functions: applying any open/closed loop transfer functions
- Calibration: converting the measurement to noise in frequency units

The beat signal is constructed by the difference in output of the PSL and the AUX Laser ($\nu 2$ and $\nu 1$ respectively in Fig. 1). In order to identify the sources contributing to the out of loop ALS noise (Fig. 2), we first need to consider all the couplings and feedback loops separately. This needs to be done for both arms separately as the loops may be the same, but the extent of noise can vary due to seismic motion acting differently or electronics noise for example.

I examined the seismic coupling in YARM, and the AUX REFL PD loop in XARM (Fig. 3).

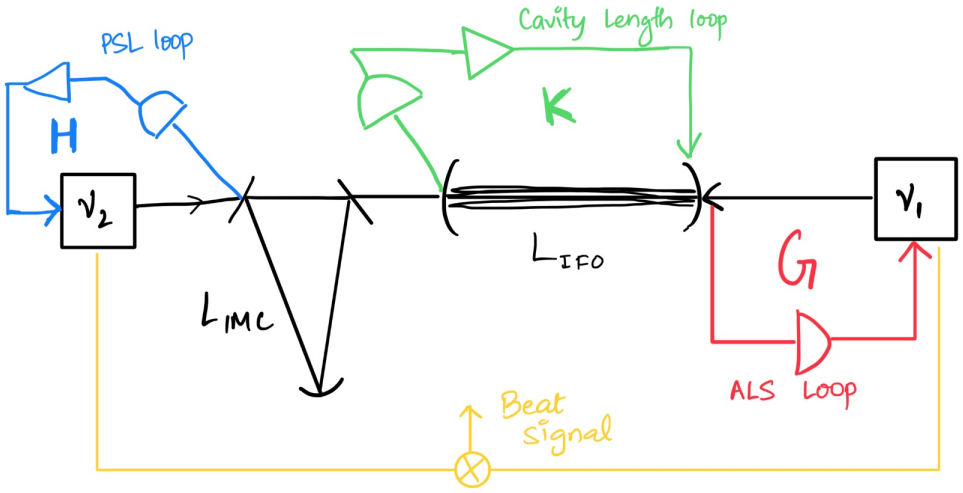

Figure 1: These are the feedback loops involved the the beat signal generation process. L-IMC and L-IFO are the lengths of the input mode cleaner and interferometer arm respectively. G, H and K are the transfer functions of the corresponding loops.

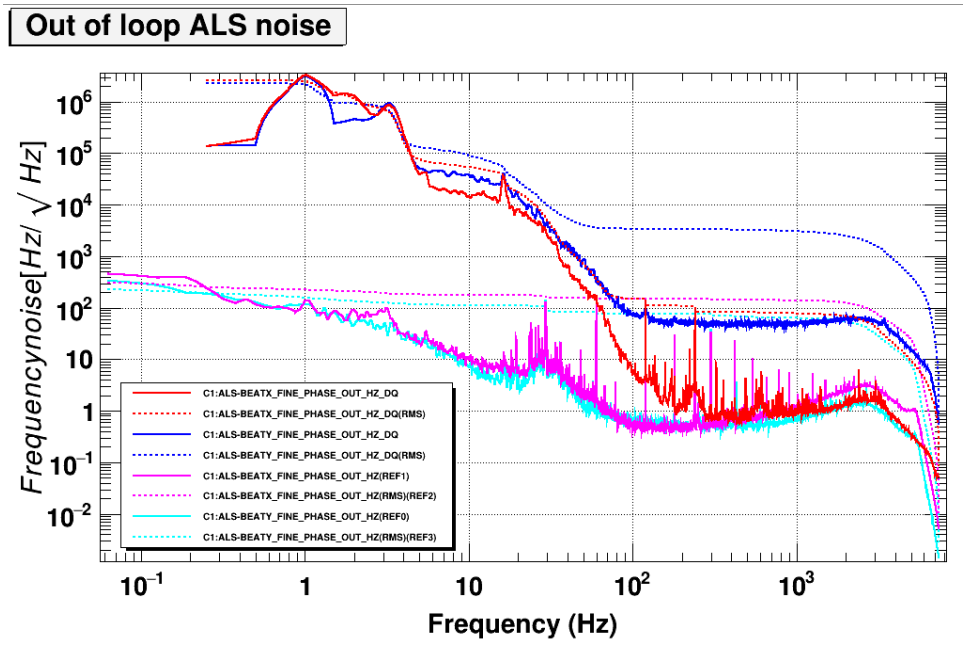

Figure 2: Out of loop ALS Noise

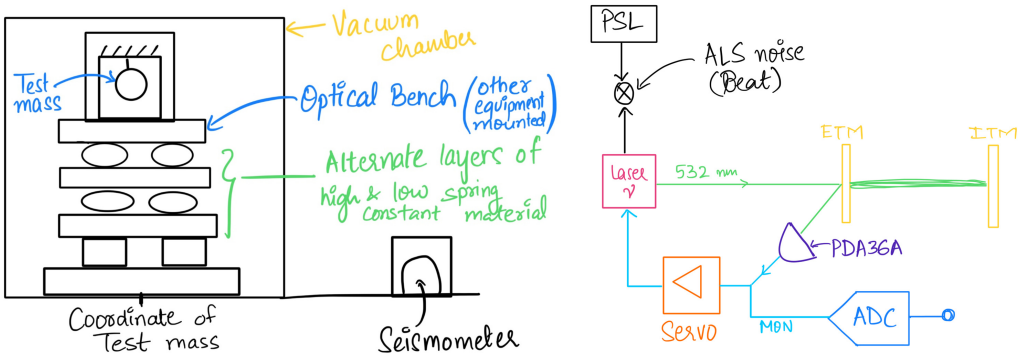

Figure 3: The left diagram is a schematic of how the seismic noise reaches the test mass. The right part is a feedback loop diagram of the AUX Laser.

4 Noise budgeting: Seismic and AUX REFL PD feedback loops

4.1 Seismic coupling

Noise budgeting the seismic part involved examining the coherence between the YBEAT and the seismometer input ie. PEM-SEIS channel. This was done by measuring the data of both the seismic channels as well as the YBEAT. I used the sitemap MEDM controls to get the relevant information such as channels names, and used NDS2 to get the data at the gps time when YARM was locked. The YBEAT is already strain data but the SEIS channel output is uncalibrated.

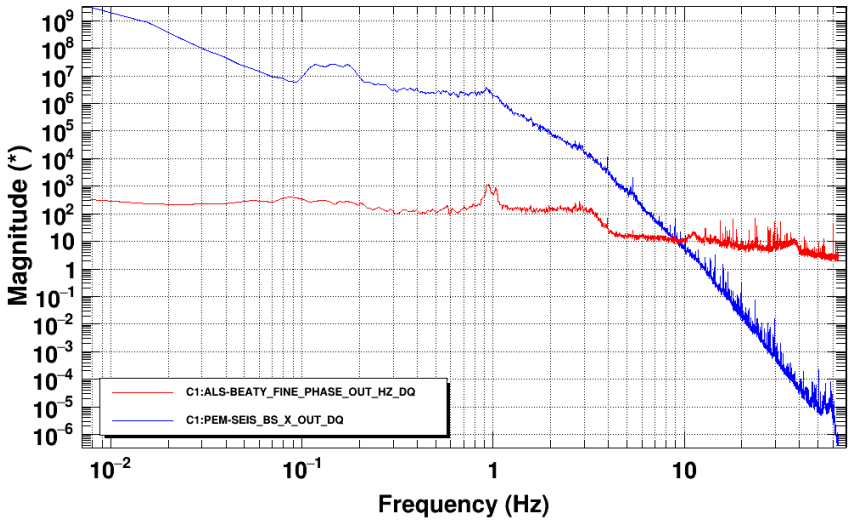

Figure 4: Seismic and Beat signal power spectral densities in units of $Hz/\sqrt{Hz}$

Calibration involves unit conversions - first we find what the seismometer actually measures using the sitemap interface, and it turns out to be the ground speed in μm/s. We can get

the displacement adding poles of the Laplace transform at 0, 1, a second order pole at 30 and use the relation $S\_L = S\_\nu * (L/\nu)$ to convert it to the units we need it in. The transfer function is calculated as per the loop configuration for that particular state while taking the measurement. The calibrated PSDs are shown in fig. 4.

4.2 AUX REFL PD feedback loop

The REFL output is the reflection of the AUX laser. It underwent an inversion at the ADC, so we changed the gain to invert it to display a positive value. We also observed an offset, blocked the REFL PD physically to check if the offset we saw on ndscope was due to the PD, but it was electronic and didn't have anything to do with the PD.

The process had 4 stages:

- ADC + PD noise. Connected the output of the REFL directly to the ADC - broke the feedback loop by disconnecting it from the servo thus not considering controls noise.
- ADC noise. Connected a 50 Ohm terminator resistor to the ADC in place of the REFL Monitor cable.
- ADC + PD + REFL noise. Connected the REFL monitor cable back to the ADC.
- Complete loop: ADC + PD + REFL + Controls noise. Closed the full loop including servo connection.
- Complete loop at a higher transmission coefficient value.

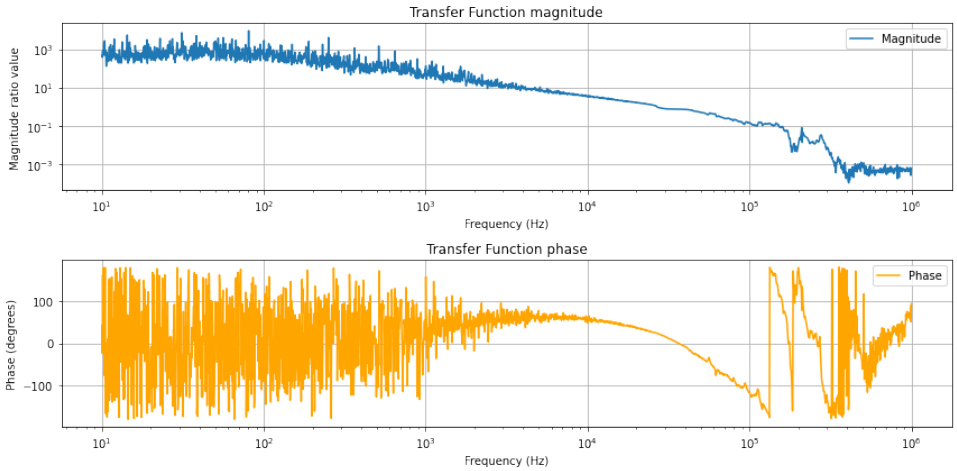

Figure 5: Bode plot of the X AUX system Open loop transfer function

To calibrate the measurements I have for the X AUX REFL PD loop, I measured the X AUX system's open loop transfer function (OLTF) by adding at injection at the error point to get the signal before and after the injection, the ratio of which gives us the OLTF (Fig.

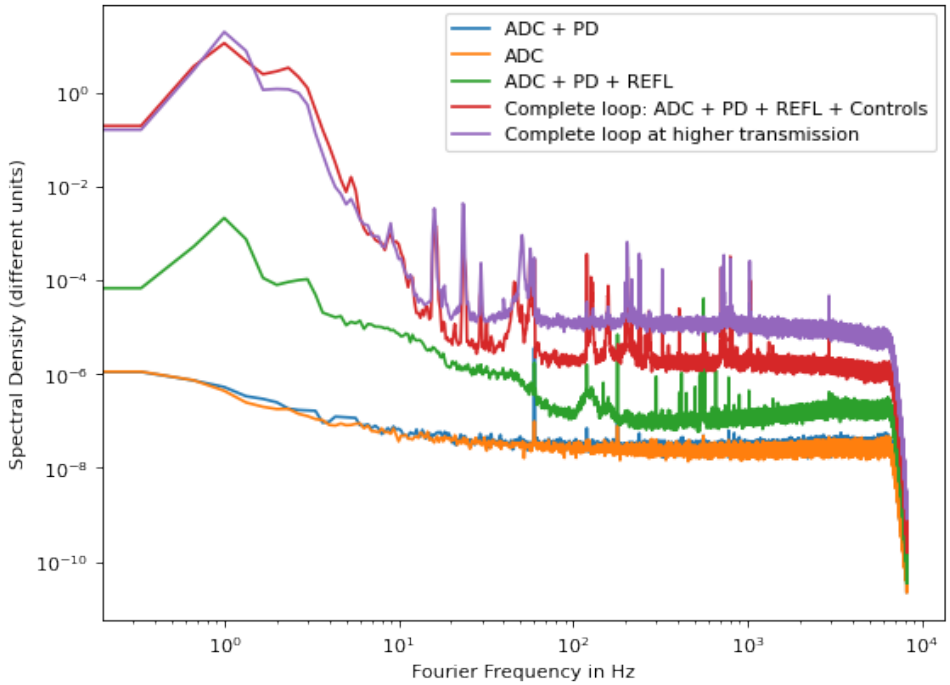

Figure 6: PSD vs Fourier Frequency for different parts of the X AUX feedback loop as indicated

5). I also took a reading of the PDH error signal to calculate the PDH Slope which I need for calibration.

The calibration is to be done from counts - as recieved through the ADC - to hertz. The ADC has a 20V range over 2^{16} bits. This allows us to convert to volts and then we use the PDH slope information to convert to Hertz. This works since the PDH slope is the ratio of the peak to peak voltage in volts and FWHM in hertz. V_{pp} was measured to be 400 mV. The calibrated plots are shown in Fig. 6.

For data acquisition and calibration of the AUX REFL PD loops, I used the Moku Go FPGA based device. I played around with the device functionalities, the implementation, and how to take readings from it. There was a major roadblock when I couldn't get the Moku to interface with the 40m laptops with linux. But I used it with the ipad and tried a couple of tasks to familiarize myself with the Moku: Measured the Johnson Nyquist noise using a 50 Ohm Terminator resistor. Measured the transfer function of a low pass filter.

I analyzed the data collected using a Python script I wrote to generate the power spectra and carry out the frequency response analysis. I also used 'diag', a command line tool developed at LIGO for doing spectrum measurements and transfer functions on the systems.

5 ALS BEAT noise contribution at 1-3 Hz

The primary objective of this analysis was to estimate the origin of the observed residual ALS BEAT contributions at 1-3 Hz, which dominate the rms of the error signals used in CARM and DARM locks. The experimental setup involved locking the PSL to IMC, locking the XARM and YARM using POX11 and POY11, and then locking XAUX and YAUX. The simplified loop models considered for analysis were the PSL to IMC open-loop transfer function (OLTF), the XARM to PSL OLTF, and the XAUX to XARM OLTF.

Main observations from the residual rms spectra indicated significant contributions from ALS BEATX and ALS BEATY at around 1-3 Hz, with notable jumps in rms at 2.2 Hz (stack resonance) and 1 Hz (pendulum resonance). These jumps, contributing to over 50% of the total rms, were investigated to estimate their origin. Initial calculations suggested that the differential normalized length fluctuations between IMC and XARM did not fully account for the observed beat noise, necessitating a more comprehensive analysis including loop effects at 1 Hz.

Incorporating loop gains into the analysis provided a clearer understanding of the residual noise contributions. The loop gains at 1 Hz were estimated as G 1e7 for the IMC OLG, H 1e9 for the XARM to PSL OLG, and P 1e5 for the XAUX to XARM OLG. The residual PSL frequency noise was found to be limited by IMC displacement noise, while the residual XARM displacement noise was limited by PSL frequency noise. The XAUX frequency noise was primarily limited by the residual XARM displacement noise, with a significant contribution from the free-running AUX NPRO noise due to the smaller XAUX OLG.

The conclusion drawn from this analysis was that the common-mode rejection is constrained by the smallest gain among the three loops, specifically the AUX laser OLG at 1 Hz. The estimated residual BEAT noise level was approximately 200 Hz/rtHz at 1 Hz, aligning with the observed noise in terms of order of magnitude. To improve common-mode rejection, it is proposed to increase the gain of the XAUX servo in the seismic band or implement seismic feedforward techniques. These adjustments aim to enhance the common-mode rejection ratio by an order of magnitude, thereby reducing the observed residual noise in the ALS BEAT measurements.

6 Sum Frequency Generation

6.1 Motivation, efficiency estimate

The future upgrade to LIGO ie. Voyager's high frequency sensitivity is achieved with high power operation and substituting unsqueezed vacuum fluctuations with a highly squeezed vacuum state. Any losses in the system provide a path for unsqueezed vacuum to couple to the readout, with small losses significantly degrading the squeezed state. Therefore, the squeezing loss budget is very strict. For the readout photodetectors (PDs), this includes a maximum allowable loss of 1%, implying very high ($\geq 99\%$) quantum efficiency (QE) at the 2 µm operating wavelength. Direct detection of IR radiation is possible with PIN junction photodetectors made from HgCdTe and InAsSb. The maximum demonstrated QE of these

detectors is of the order of 90% and will need improvement for use in Voyager.

Sum-frequency generation (SFG) provides an alternative path for high QE photodetection. By mixing a strong (e.g. resonantly enhanced) pump, for example at 1064 nm, the 2 µm fields may be upconverted to 700 nm. After upconversion, traditional InGaAs or Si PDs may be used to achieve $\geq 99\%$ QE. Light upconversion for improved photodetection. In the case of resonant SFG, even a modest finesse (< 1000) cavity providing optical gain for the pump wavelength may reach a quantum efficiency of $\geq 95\%$. With further R&D, such upconversion quantum efficiencies may approach $\geq 99.9\%$, matching external QE values attainable with Si devices.

Crystal materials lacking inversion symmetry can exhibit a so-called nonlinearity. In such nonlinear crystal materials, second order effects such as Sum Frequency Generation ie. SFG, or difference frequency generation ie. DFG can occur, where two pump beams generate another beam with the sum or difference of the optical frequencies of the pump beams. Second order nonlinear processes require phase matching to be efficient. Usually there is no simultaneous phase matching for multiple processes, so that only one of them can take place.

SFG is a parametric process, meaning that the photons satisfy energy conservation: $\omega_3 = \omega_1 + \omega_2$, where ω_3 is the sum frequency (SF) and ω_1, ω_2. are the fundamental pump frequencies. Voyager uses a signal of 2 um, so at the output of the GW detection, the pump used will be a 1064-nm Nd:YAG laser, resulting in an upconverted signal output at 700 nm.

A special case of sum-frequency generation is second-harmonic generation, in which $\omega_1 = \omega_2$. This has been done before at the Quantum Interferometry Lab, where I worked on replicating it to complete pump alignment because in second-harmonic generation, only this one input light beam is required. If $\omega_1 \neq \omega_2$, two simultaneous beams are required, which can be more difficult to arrange at the outset.

The efficiency of the conversion process for a waveguide of length L with negligible propagation loss and a phase-matched interaction is given by

$$\eta = \sin^2\left(\sqrt{\eta_{\text{nor}} \cdot P_p \cdot L}\right)$$

where P_p is the pump power. The normalized efficiency η_{nor} is given by

$$\eta_{\text{nor}} = \frac{\varepsilon_0^2 \cdot d_{\text{eff}}^2 \cdot |\theta_Q|^2 \cdot 2\omega_1\omega_2 \cdot Z_0^3}{n_1 \cdot n_2 \cdot n_p}$$

where d_{eff} is the effective nonlinear coefficient, $Z_0 = \sqrt{\frac{\mu_0}{\varepsilon_0}}$ is the impedance of free space, n_j are the effective indices of refraction, and θ_Q is the mode-overlap integral for three-wave interactions.

I wrote a python code to compute this efficiency as a function of pump power as shown in fig. 19.

6.2 Second Harmonic Generation setup

The Second Harmonic Generation (SHG) setup was initially configured by another lab member Shoki. This involved a single laser of wavelength 1064 nm as input to a PPKTP crystal,

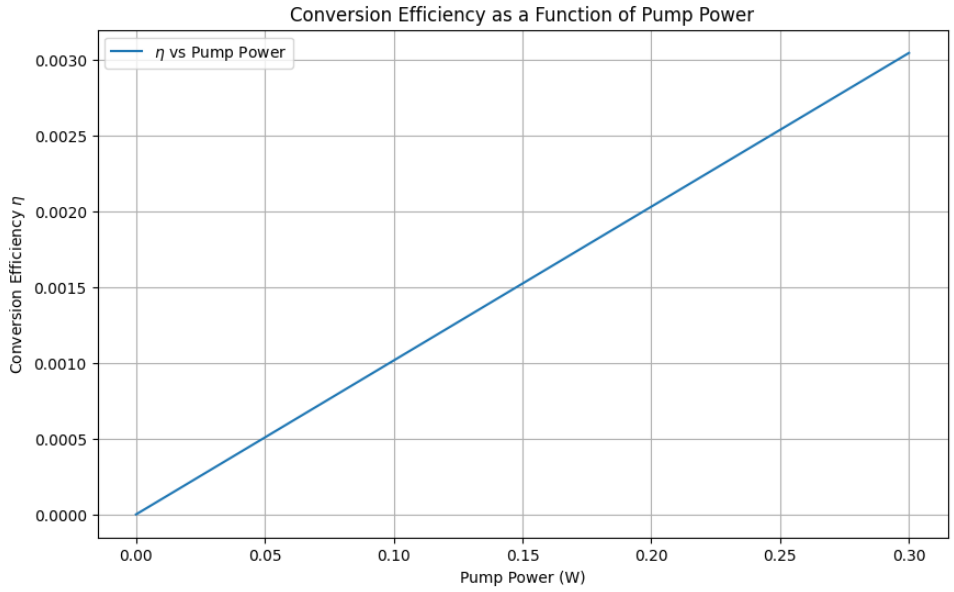

Figure 7: Efficiency as a function of pump power. Through the function is a sine squared, it is linear at low power.

observing an SHG output of 532 nm light.

Using this as a basis, I drew up a schematic (fig. 8) for Sum Frequency Generation. The pump (1064 nm) will be the same one currently in use for the SHG - a Diabolo Laser. It is placed on the other side of the table where the setup for another experiment ie. WOPA is. After clearing the table of other unused mounts and optics, I cleaned the SHG related optics using Isopropyl alcohol and changed the first mirror mount to a transparent one that allowed me to see if the beam was centered and aligned before sending it to the other side of the table.

The 1064 nm laser beam power and beam profile were measured using a DataRay beam profiler. Laser power was measured at three different points and found to be as follows:

- Before the half-wave plate: 309 mW
- After the polarizing beam splitter on the WOPA side: 9 mW
- After the polarizing beam splitter on the SFG side: 300 mW

The beam profiler initially faced issues detecting the cameras, but this was resolved by rebooting the laptop and the DataRay application. The beam was found to be diverging, with the beam waist appearing to be inside the Diabolo box. To accurately determine the beam waist and its position, I fitted the beam width data to a hyperbolic model. In this model, the horizontal axis (x) represents the distance from the laser (Rayleigh range) and the vertical axis (y) represents the beam width. The hyperbolic equation used is:

$$y = b^2 + \left(\frac{x}{z_0}\right)^2$$

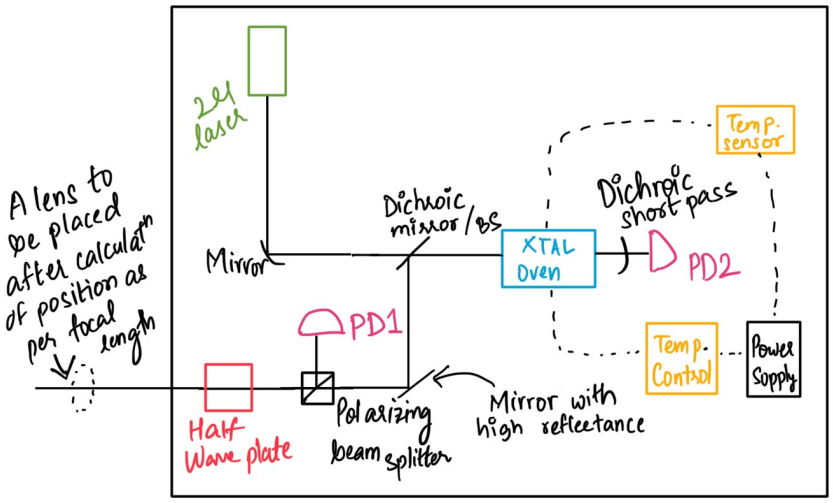

Figure 8: Schematic for the setup to observe Sum Frequency Generation

where b is the beam waist, and z_0 is the Rayleigh range.

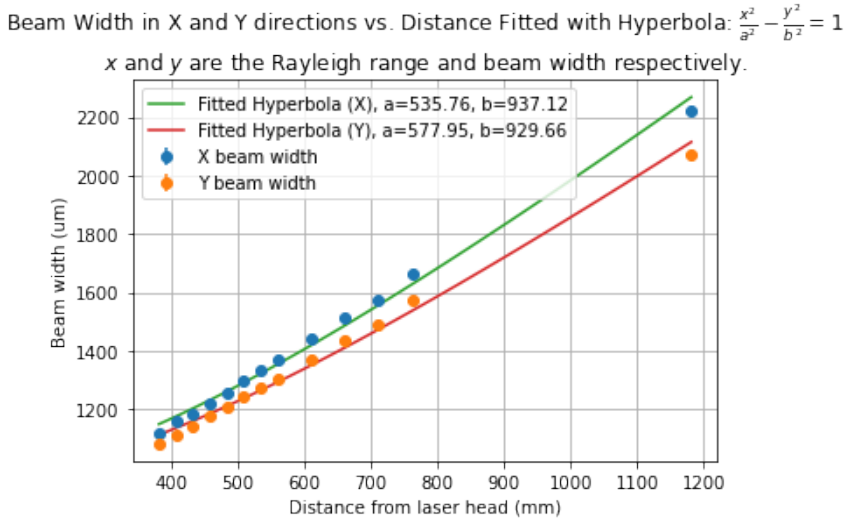

Figure 9: Fitting of beam width data to a hyperbolic model.

The beam width data was used to fit the hyperbola, assuming the initial beam waist was positioned at the laser (i.e., $x = 0$), as shown in Fig. 9. The fitted hyperbola indicated an initial beam waist of approximately 0.9 mm.

The PPKTP crystal damage threshold at 1064 nm is 260 MW/m^2. To ensure safe operation, the target beam waist was estimated, keeping in mind the crystal damage threshold and the oven opening size. Figure 10 is a plot of the minimum beam waist as a function of pump power, which indicates that a beam waist above 25 microns would be safe for the crystal.

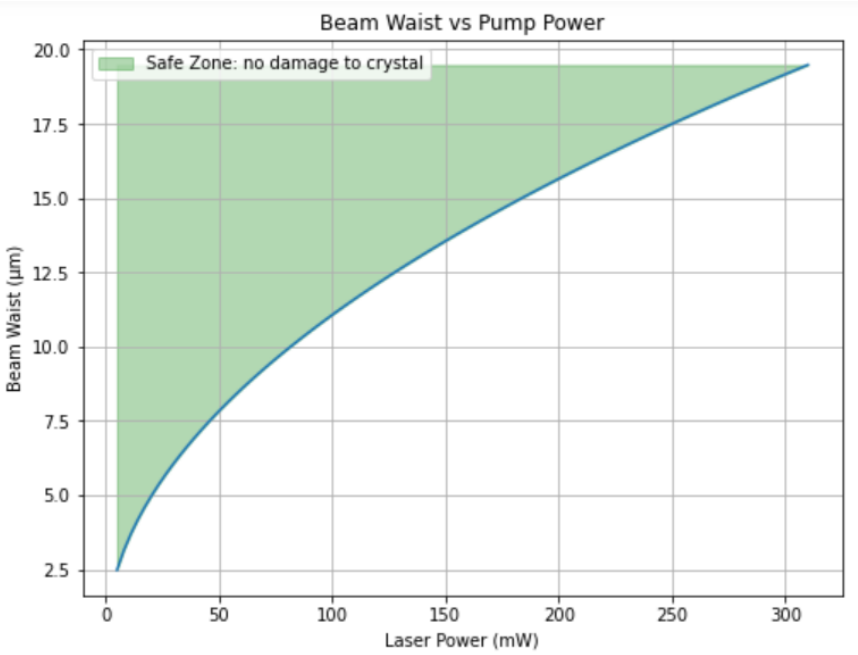

Figure 10: Minimum (safe) beam waist as a function of pump power.

6.3 Mode Matching and Alignment

Mode matching was conducted to achieve the desired beam waist at the oven position (87-88 inches from the laser). The q parameter is a complex number that describes the beam's curvature and spot size at a given point. For a Gaussian beam, the q value at any position z can be expressed as:

$$q(z) = z + iz_0$$

where z_0 is the Rayleigh range, which is related to the beam waist w_0 by:

$$z_0 = \frac{\pi w_0^2}{\lambda}$$

After calculating the initial and target q values using the corresponding beam waist values and positions, the ABCD matrix equation for transformation can be written out and calculated to find the positions of the lenses to be used. For a system of multiple lenses and free space propagation, the overall ABCD matrix is the product of individual matrices.

Using an online Mode-Matching Calculator as shown in fig. 11, I procured an initial estimate of the lens positions. After testing various lens combinations, lenses with focal lengths of 150 mm and 75 mm were selected. However, there was a power loss of 20% detected due to the 150 mm lens, so I replaced it with a 175 mm lens to minimize power loss till another 150 mm lens was found.

Alignment was achieved using two steering mirrors to control the two parameters - beam's incidence angle and position on the crystal. The final lens positions were: f = 250 mm at 36.5 inches and f = 150 mm at 63 inches from the laser head. The setup is shown in fig.

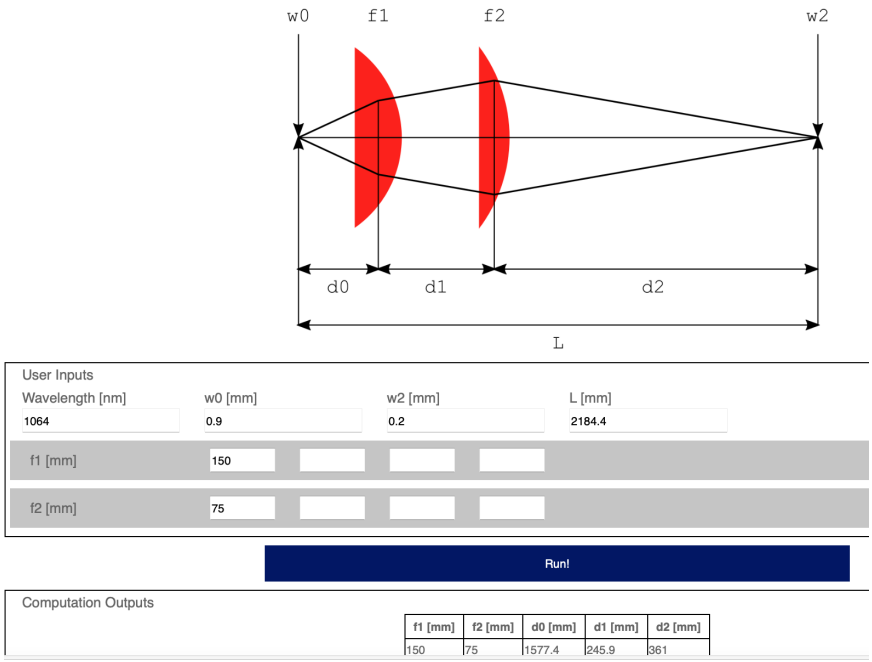

Figure 11: Mode matching using 2 lenses to estimate the positions of the lenses and get the required waist at the oven

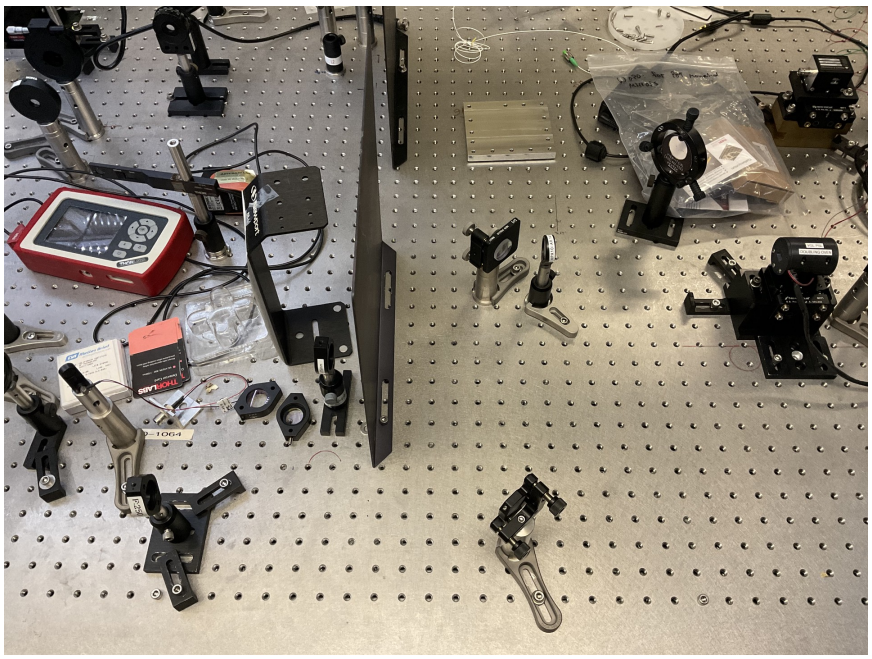

Figure 12: Mode matched and aligned SHG setup achieved

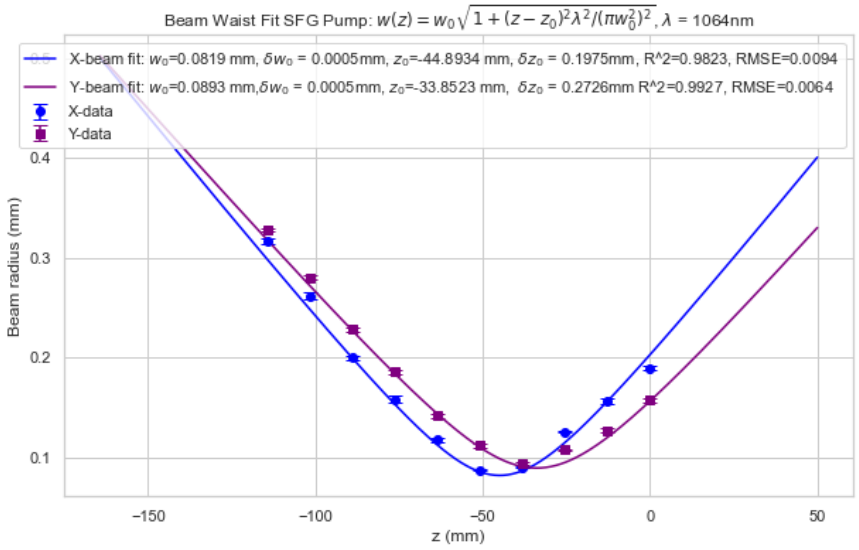

Figure 13: Gaussian beam fit after placing lenses to achieve mode matching

12. The beam was profiled again and the gaussian beam fit is shown in fig. 13, indicating a beam waist of 50 micron at the oven.

I placed a dichroic beam splitter after the crystal oven, which was reflective to 1064 nm and transmissive to 532 nm. A photodetector PDA10A was also placed to detect the green light at the output.

7 Characterizing SHG output

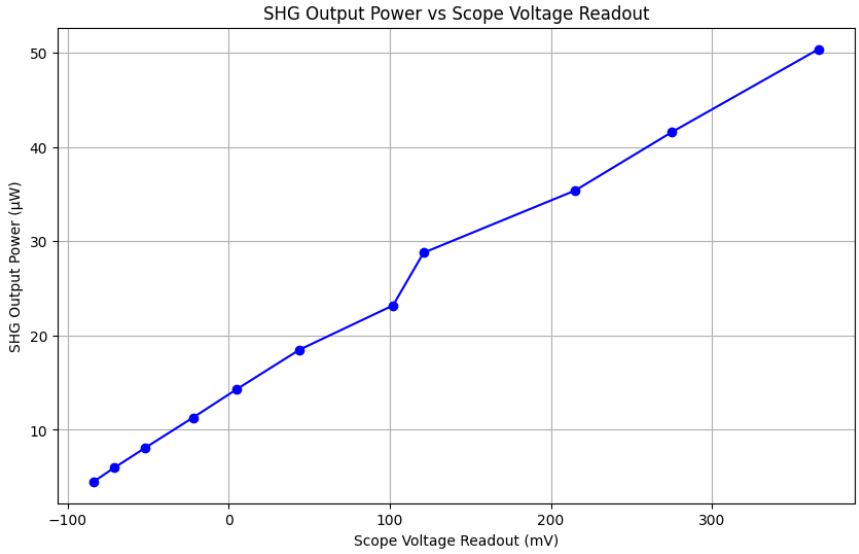

Figure 14: Oscilloscope Voltage to Output Power calibration.

Voltage that we read out on the oscilloscope connected to the PD corresponds to the output power at that point. This was calibrated and the plot is shown in fig. 14

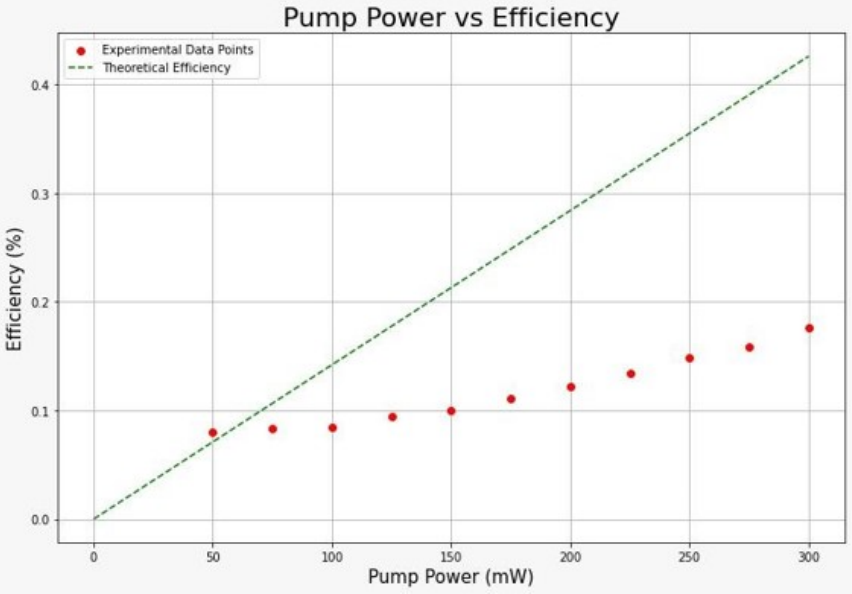

Figure 15: Theoretical and measured SHG output efficiency as a function of pump power.

The SHG output power shows a clear correlation with the pump power. By measuring the output power as a function of the input pump power, valuable insights can be gained to optimize the upconversion efficiency. The pump power was varied using a half-wave plate, and the corresponding output power was recorded as voltage on the oscilloscope. Figure 15 presents the theoretical and measured SHG output efficiency as a function of pump power. A noticeable discrepancy in the efficiency values, particularly at higher pump powers, was observed. After checking the polarization of the pump beam, it was confirmed that the polarization needed optimization to account for this difference.

Given the inaccuracy of the oven controller readout, three robust temperature readout methods were explored: 1. A sensor consisting of a complex circuit 2. Thorlabs TED200C 3. A resistor-based readout

After spending a while trying to configure the other options, finally a simple temperature readout setup was implemented using a 5.1 K Ohm resistor, which was then calibrated using 3 temperature points of reference. The calibration curve for the readout is shown in fig. 16

Fig. 17 illustrates the relationship between the output power and the crystal temperature, showing how efficiency is influenced by temperature variations. The output power remains relatively stable at lower temperatures but begins to increase significantly around 35°C, peaking at 37.2°C. This peak corresponds to the highest efficiency observed, where the system remains first-order insensitive to small temperature fluctuations, ensuring stable operation even with minor environmental changes.

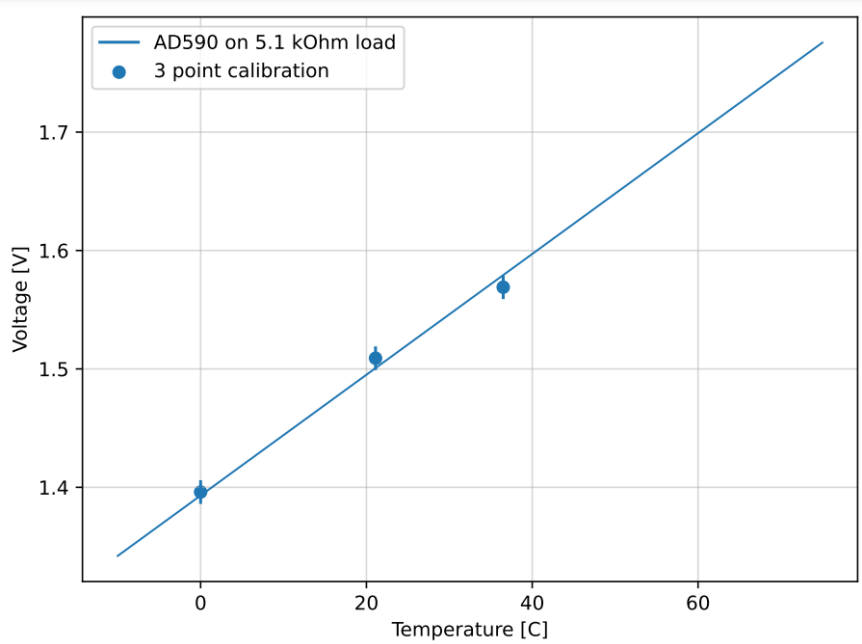

Figure 16: Calibration curve for the temperature readout, assuming 0.2 error in room and body temperatures.

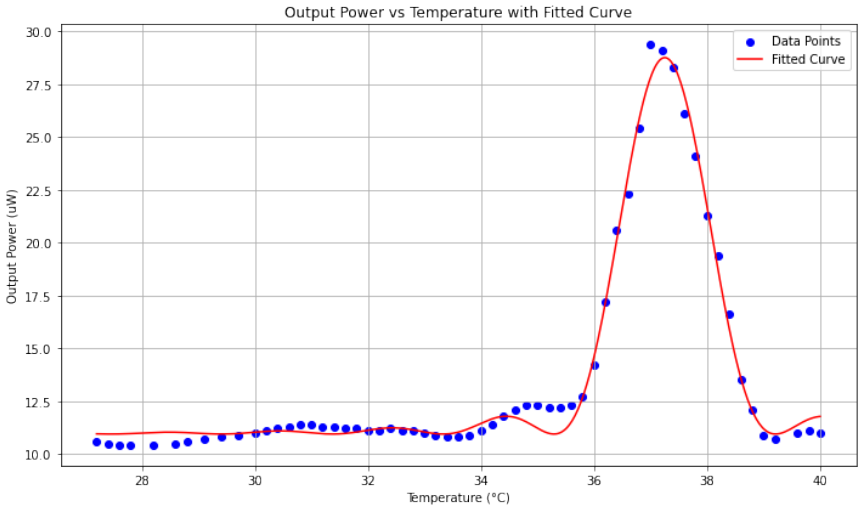

Figure 17: SHG output power vs crystal temperature

8 Single pass of Sum Frequency Generation

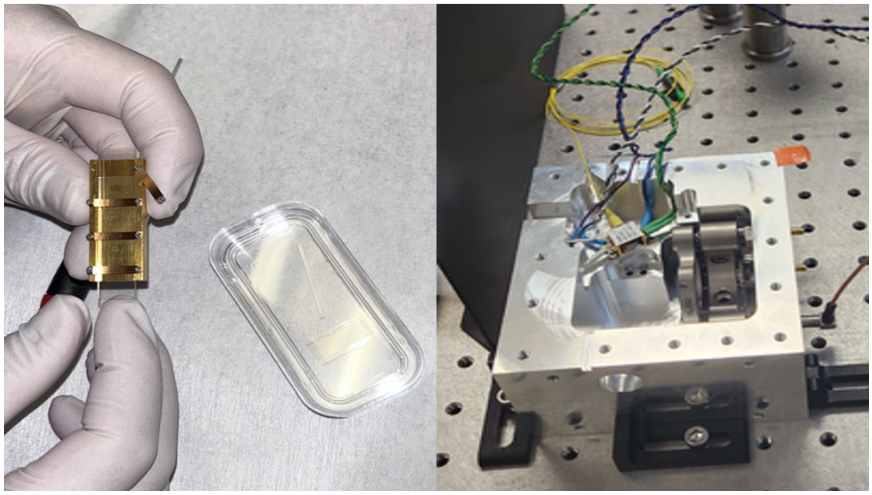

Figure 18: KTP crystal replaced by PPLN, ECDL set up for the signal beam

To facilitate the transition to Sum Frequency Generation, we replaced the KTP crystal with a periodically poled lithium niobate (PPLN) crystal (Fig. 18). PPLN offers higher nonlinear coefficients and crystal damage threshold, making it more suitable for efficient SFG at 2 µm. In parallel, we profiled the signal beam emerging from the external cavity diode laser (ECDL) to ensure its optimal waist for the SFG process. The beam's spatial profile was analyzed using a beam profiler. These measurements were crucial to ensure that the signal beam was well-suited for efficient interaction with the pump beam inside the PPLN crystal. The mode matching was done to ensure that the signal waist is slightly smaller than the pump beam.

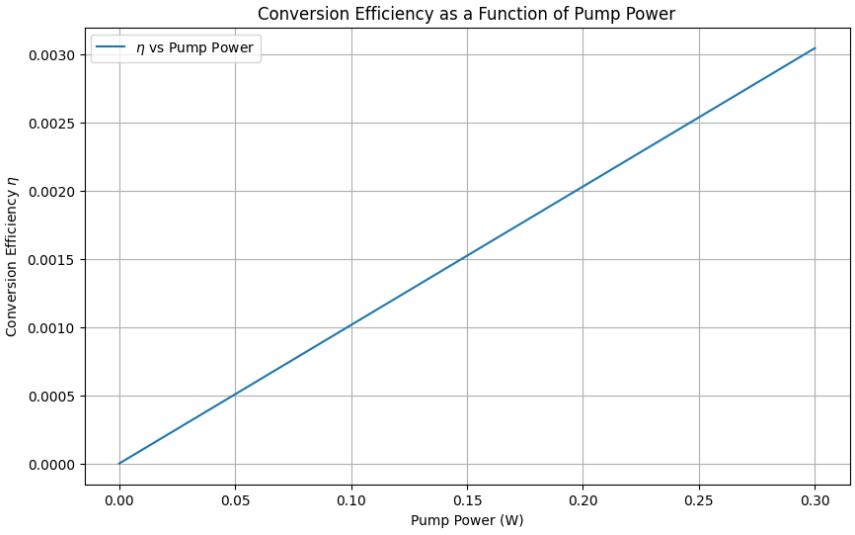

Figure 19: SFG Efficiency as a function of Pump power

There is ongoing effort dedicated to achieving the first pass of Sum Frequency Generation (SFG). Figure 19 presents the theoretical Sum Frequency Generation (SFG) efficiency as

a function of pump power. As expected, the efficiency increases steadily with increasing pump power, following a typical nonlinear behavior. At lower pump powers, the efficiency is relatively low due to insufficient photon interaction within the nonlinear medium. However, as the pump power increases, the efficiency rises sharply, reaching a saturation point (not shown in fig.) after which further increase in pump power result in diminishing returns.

9 Other areas of focus

9.1 Locking of the LIGO 40m interferometer

Locking of the 40m interferometer arms and ALS is done from the control room using the MEDM 'sitemap', which has screens which let us interface with the interferometer remotely. There is a specific order followed to lock the IFO efficiently. I have worked on familiarising myself with these different controls and basic steps to lock the interferometer.

9.2 Vacuum pressure checker

The vacuum system in the 40m LIGO requires liquid nitrogen to hold the pressure at about 70 psi. These liquid nitrogen tanks last for about 2 to 3 days and need to be replaced regularly. There is a danger to the system if the pressure falls low due to the Nitrogen tanks not being replaced. I wrote a python script which acts as a checker to send out a notification when the pressure falls below a certain threshold.

References

[1] https://doi.org/10.48550/arXiv.2005.02531

[2] Karl Johan Astrom, Richard M. Murray, Feedback Systems: An Introduction for Scientists and Engineers

[3] Notes on the Pound-Drever-Hall technique, LIGO Technical Note (1998), https://dcc.ligo.org/public/0028/T980045/000/T980045-00.pdf

[4] Gautam Venugopalan, Prototype Interferometry in the Era of Gravitational Wave Astronomy, https://thesis.library.caltech.edu/14288/3/main.pdf

[5] A Cryogenic Silicon Interferometer for Gravitational-wave Detection, https://arxiv.org/pdf/2001.11173

[6] Long-wavelength-pumped upconversion single-photon detector at 1550 nm: performance and noise analysis, https://opg.optica.org/oe/fulltext.cfm?uri=oe-19-22-21445&id=223665

[7] Improvement to Sellmeier equation for periodically poled LiNbO3 crystal using mid-infrared difference-frequency generation, https://www.sciencedirect.com/science/article/pii/S0030401806006778